IEEE Access
Multidisciplinary | Rapid Review | Open Access Journal

Received April 28, 2020, accepted May 7, 2020, date of publication May 21, 2020, date of current version June 11, 2020.

Digital Object Identifier 10.1109/ACCESS.2020.2996366

Analysis of Automotive Lidar Sensor Model Considering Scattering Effects in Regional Rain Environments

MIJUNG BYEON AND SANG WON YOON, (Senior Member, IEEE)
Automotive Engineering Department, Hanyang University, Seoul 04763, South Korea

Corresponding author: Sang Won Yoon (swyoon@hanyang.ac.kr)

This work was supported by the National Research Foundation of Korea (NRF) grant funded by the Korea government (MSIT) under Grant 2020R1F1A1069925.

ABSTRACT Automotive Lidar sensors are highly susceptible to their environment. One of its major limitations results from the effects of rain environments, which should be seriously considered while designing a Lidar system. This study addresses the impact of rain on the Lidar system by considering the raindrop distributions of different regions. The regional distributions are derived from the rainfall data of three locations, which were reported by previous works, and converted using the constrained-gamma model. The regional distribution reveals different characteristics of raindrops, such as sizes, shapes, and numbers. The derived raindrop distributions are imported to a custom-built Lidar model, providing three models representing the three regions. The simulation results demonstrate that the signal power received by a Lidar attenuates, which is modeled using Mie scattering theory, and the amount of attenuation clearly differs in the regional models. Therefore, the attenuation characteristics change according to the regions; consequently, their effect on the Lidar sensor performances are quantitatively evaluated. In addition, the custom-built Lidar model is mounted on a virtual vehicle, which is simulated using a commercial automobile testing software, PreScan. The driving simulation also demonstrates similar conclusion that the regional raindrop distribution is critical in determining the Lidar performances.

INDEX TERMS Automotive Lidar, constrained-gamma model, Mie scattering, raindrop axis ratio, raindrop distribution.

I. INTRODUCTION

The recent advancements in automotive electronics have resulted in safer and more convenient vehicles. An advanced driver assistance system (ADAS) is one of the core electronic systems, whose performance is strongly determined by ADAS sensors. Typical ADAS sensors include ultrasonic sensors, cameras, radio detection and ranging (Radar), and light detection and ranging (Lidar) systems. Lidar sensors are usually mounted on the roof of the vehicle and provide information regarding the objects surrounding a vehicle using laser pulses. Lidar sensors are critical to recognition algorithms of ADAS and autonomous vehicles and are essential in path planning and reactive control of autonomous vehicles [1]. Lidar data are often sensor-fused with other ADAS sensors, such as cameras and/or Radar [2], [3]; moreover, they are sometimes co-used with other automotive sensors, such as a global positioning system or inertial measurement unit [4]. However, the current Lidar sensors have several limitations including high cost, bulky size, and robustness issues. Another major drawback is that Lidar sensors are relatively susceptible to weather conditions, including rain, snow, and fog.

In particular, rain environments are known to seriously degrade the performance and reliability of Lidar sensors. Lasers are readily reflected or scattered by encountered particles and experiences serious signal attenuation; this results in Lidar sensor errors. The sensor errors bring in reliability issues in automotive systems that use these sensors [5]. Thus, the Lidar signal distortion by rain has been actively investigated; most studies have focused on the experimental results when Lidar sensors were exposed to rain or a test setup with simulated rainfall [5], [6]. Several recent efforts attempted to define comprehensive models explaining Lidar under rainfall conditions. A previous paper overviewed several physical principles required to describe laser signal disturbance and

The associate editor coordinating the review of this manuscript and approving it for publication was Atif Iqbal.

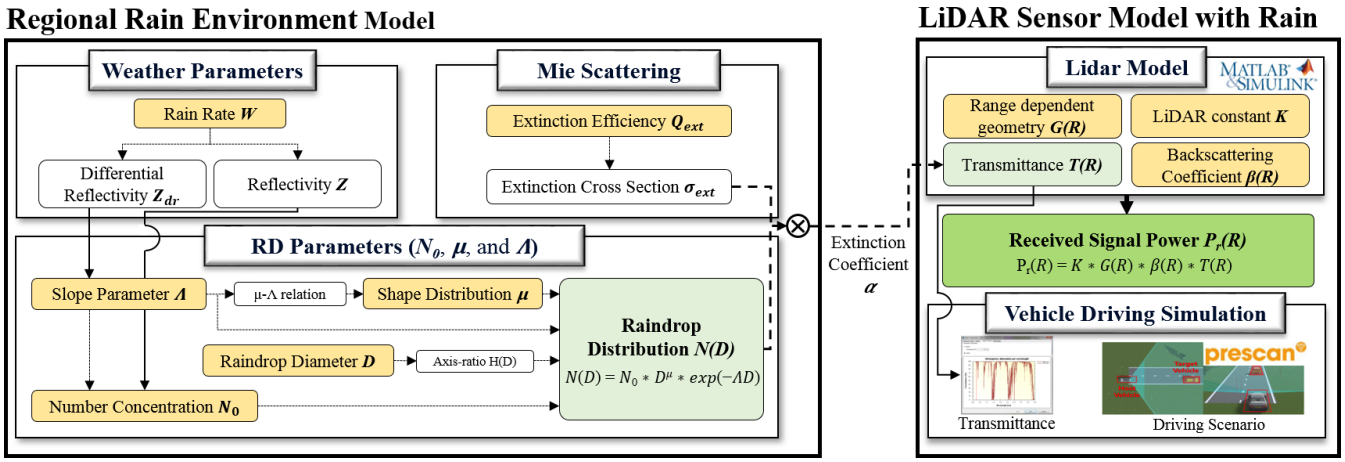

FIGURE 1. Overall block diagram of the concepts considered in the proposed model.

presented key theoretical backgrounds using self-developed transmission models [6].

The overviewed principles were explained by presenting basic probabilistic models for key rainfall parameters [7]. In this work, adverse rainfall effects on Lidar sensor were modeled using the Mie scattering theory and Monte Carlo simulation framework; further, an efficiency coefficient was specified as the key parameter.

These analytic processes require individual models of raindrops and Lidar sensors. Raindrops were randomly distributed inside the laser propagation path and their effects were displayed based on the relationship between the aperture diameter and the transmitting power [8]. Here, a probability density function of raindrop diameter was employed. Similarly, a Lidar test methodology was designed considering the raindrop distribution [5]. Spherical water drops were studied to understand the effects of rain and fog [9]. In this study, rain or fog drops are uniformly distributed, and absorb and scatter electromagnetic waves depending on their size. Moreover, for a specific drop size, the performance degradation of the camera, Radar, and Lidar can be compared using the efficiency coefficient. Another paper considered a rain distribution model called the three-parameter lognormal distribution to compare the rainfall effect on the camera, Radar, and Lidar [10].

Though, a research that incorporates a more realistic rain environment is still required. For example, a raindrop distribution analysis should incorporate parameters other than raindrop size and numbers, such as raindrop shape and rain rate. Thus, it is important to introduce regional raindrop distributions based on meteorological data and determine the regional impact on Lidar performances. However, to the best of our knowledge, such a work has not yet been reported for automotive Lidar sensors.

The Lidar sensor models are critical components; consequently, it is important to consider their influences on automotive systems. The adverse effects of rainfall result in sensor errors, which may lead to severe accidents [10]. Conversely, the system may not respond to the errors if they are negligibly small. Therefore, the sensor errors should be quantitatively expressed for automotive systems, such as ADAS. However, there are not many quantitative studies on the effects of rain on ADAS performances. A recent paper proposed a mathematical Lidar model showing its degradation as a function of the rate of rainfall [11]. The model was then used in an obstacle-detection system relying on Lidar point cloud algorithms. However, the rainfall effect was not fully incorporated because the proposed equation was a function of only the rain rate and did not consider other important raindrop characteristics.

In this work, the raindrop characteristics were determined using the rainfall data at different locations. The regional characteristics provided the raindrop sizes, numbers, and shapes as a function of the rain rate. The regional raindrop distributions were defined by constrained-gamma (CG) models, and the rain-induced attenuation was expressed using Mie scattering theory. They were converted to an extinction coefficient, which was incorporated in a custom-built Lidar sensor model, and the LiDAR performances corresponding to different regions were compared. In addition, the Lidar sensor outputs were inputted to a vehicle driving simulator and their impact on the system was quantitatively analyzed.

II. MODELING CONCEPT

Figure 1 illustrates an overview of the proposed models and simulation processes. We developed three major simulation models. First, the rain environments were modeled. The rain model consisted of two parts representing the scattering effect by a particle and the regional raindrop distribution. The scattering effect was derived using Mie scattering theory, which is suitable for water vapors, and expressed by the extinction efficiency Q_{ext}. Q_{ext} was then converted to an extinction cross section σ_{ext}. The raindrop distributions were individually defined based on the region, which consisted of varying sizes, numbers, and shapes of raindrops. The regional raindrop information was extracted from the rainfall data measured at

three locations in Asia, North America, and Pacific Ocean. To define the raindrop information, several measured parameters were predetermined. The used parameters were reflectivity, Z, and differential reflectivity, Z_{dr} which depend on the rain rate. Z and Z_{dr} were converted to other raindrop parameters, including number concentration (N_o), slope parameter (Λ), and shape distribution (μ). It is to be noted that each raindrop parameter has a different dependency on Z and/or Z_{dr}. Their dependency is shown in Fig. 1. The equivalent volume diameter, D, was calculated from the measured rain data. Thus, the raindrop distribution function $N(D)$ could be quantified.

The extinction coefficient and raindrop distribution function were multiplied to determine the extinction coefficient α, which represents the degree to which the Lidar sensor is disturbed by rain. Note that the rain parameters differ according to the regions; consequently, the amount of Lidar disturbance also differs based on the regions. The regional raindrop distribution was then imported to the Lidar sensor model. The Lidar sensor model was custom-built using MATLAB & Simulink software; moreover, it consists of all the parameters required to exploit the Lidar governing equation. The Lidar parameters considered are transmittance $T(R)$, Lidar constant K, backs0cattering coefficient $\beta(R)$, and range dependent geometry $G(R)$. Here, the variable R is the distance between the Lidar sensor and its targeting object. The Lidar sensor model is affected by the imported rain environment model, which is expressed by the attenuation in the received power. In addition, an automobile driving model was built and evaluated using the PreScan software. The commercial software already contains vehicle conditions and basic Lidar sensor settings. By inputting the information regarding the rain-disturbed Lidar model, the software was able to demonstrate the effects of rain on vehicle driving performance.

These models and simulations clarified the rain effects on Lidar performance and their dependency on regions. These were quantitatively evaluated at both sensor and vehicle system levels.

III. THEORY FOR RAIN ENVIRONMENT

A. RAINDROP SIZE DISTRIBUTION

Raindrop size distribution (RSD) indicates the distribution of the concentration of raindrops according to the unit particle size in a given unit volume ($mm^{-1}m^{-3}$). This is significantly diverse because it reflects the characteristics that are demonstrated when raindrops fall in the atmosphere.

There are many different methods of RSD retrieval [12]–[14]; however, we used the constrained gamma (CG) method [14] relying on reflectivity and differential reflectivity data measured from raindrop measurements. The reflectivity Z is measured from the signals reflected from the raindrops, indicating the degree of reflection in the raindrops. The differential reflectivity Z_{dr} is determined by the average shape of the raindrop within the weather observation range [15]. The reflectivity and differential reflectivity were derived using the rain rate estimation algorithm [16], as given below:

$$W\,(Z) = 0.0365 \times Z^{0.625} \tag{1}$$

$$W\,(Z) = 1.70 \times 10^{-2} \times Z^{0.7143} \tag{2}$$

Here, $R(Z)$ indicates the rain rate according to the degree of reflectivity. Note that the formulas differ by regions because they are curve-fitted using rain data at specific locations. Equations (1) and (2) are based on the data measured at Daegu, South Korea [13] and Florida, United States of America [17], respectively.

Next, the relationship between rain rate and differential reflectivity was calculated by using the equation of Bringi and Chandrasekar [16].

$$W\,(Z, Z_{dr}) = 6.70 \times 10^{-3} \times Z^{0.927} \times Z_{dr}^{-3.43} \tag{3}$$

$W(Z, Z_{dr})$ indicates the amount of rain rate according to the differential reflectivity. Equation (3) are used in both of the references [13], [17].

B. RSD PARAMETERS BY REGIONS

To calculate RSD parameters, we need to consider a probability model. The used model is the gamma model derived by Ulbrich (1983) [18], which presented a relation as given below:

$$N\,(D) = N_0 D^{\mu} exp\,(-\Lambda D) \tag{4}$$

The parameter $N(D)$ indicates the concentration distribution of the equivolume diameter of raindrops in an interval $[D,\ D + \delta D]$. The parameter D indicates the diameter of spherical raindrops per unit volume. The gamma distribution consists of three parameters: μ, Λ, and N_0. The parameter N_0 indicates the concentration of the gamma RSD. The parameters μ and Λ indicate the shape parameter and the slope of distribution, respectively. These three parameters, which are components of the gamma function, are a dependent relationship between each other. However, several works demonstrated that there was a correlation between μ and Λ, and derived an empirical μ - Λ relationship [16].

$$\mu = -0.0201\Lambda^2 + 0.902\Lambda - 1.718 \tag{5}$$

This μ - Λ relationship enables the CG model to be presented as a two-parameter RSD [19]. The data measured at Daegu [13] does not mention the μ - Λ relationship, but we assume the same equation can be employed. The Λ in (5) is calculated as follows [20]:

$$\Lambda = 0.0125Z_{dr}^{-3} - 0.3068Z_{dr}^{-2} + 3.3830Z_{dr}^{-1} + 0.1790 \tag{6}$$

The Z_{dr} value is obtained from (3), using the Z value defined from (1) or (2), depending on regions. The Λ determines the shape parameter μ of the RSD using (5). Then, N_0 is calculated using the Λ and (7).

$$N_0 = Z_{hh} \times 10^{(0.00285Z\Lambda^3 - 0.0926\Lambda^2 + 1.409\Lambda - 3.764)} \tag{7}$$

The parameter Z_{hh} indicates the reflectivity of vertical polarization. Therefore, the RSD at specific regions can be implemented using the calculated parameters and the diameter D of the raindrop. As described, regional RSD can be determined using the three parameters obtained from (5), (6), and (7). The RSD includes raindrop size and distribution information, but does not consider raindrop shapes whose impact is also critical.

C. RAINDROP SHAPE – RAINDROP AXIS RATIO

Typical RSD does not include raindrop shape information, which is also considered in this study. Herein, the shape of the raindrop is represented as its axis ratio. In general, we understand that raindrops have a spherical shape. However, raindrops actually vary in size and shape, and vary depending on the region [13], [17], [21], [22]. If the diameter of a raindrop is less than or equal to 1 mm, it normally looks similar to a sphere; further, it is split into small diameter raindrops if the diameter is more than 4 mm [23]. As shown in Fig. 2, a diameter of 4 mm or more is hardened by the air pressure, and the central part of the raindrop becomes gradually dented and breaks into small raindrops as it is unable to overcome the air pressure. These split raindrops become spherical.

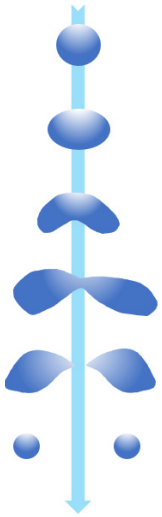

FIGURE 2. Process of breakup in a raindrop.

This phenomenon occurs owing to the surface tension of the raindrops and the air pressure. In the case of water, small raindrops have a sufficient surface tension to maintain a spherical shape; however, as the size increases, the surface tension decreases, and the shape of raindrop becomes oblate [24]. Therefore, it is known that actual raindrops are spherical when they are small, but as they grow in size, they become increasingly oblate.

However, it is more difficult to calculate the scattering of the oblate raindrop when compared to the spherical raindrops. A previous work presented a method to determine scattering by oblate particles of different sizes [25]. A follow-up work calculated the extinction for spheroids of different sizes,

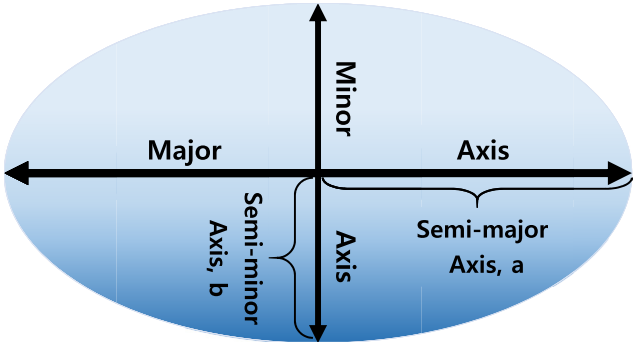

FIGURE 3. Shape configuration of a raindrop.

shapes, and refractive indices within a variety of environments [26]. This work employs the equivalent sphere diameter (ESD) concept and a spheroid raindrop is approximated to be a spherical raindrop having the same volume, assuming that they have equivalent scattering effects.

As shown in Fig. 3, the spheroid has two lengths, which are called as the major axis and minor axis. The major axis is the lateral axis of a raindrop; moreover, half of its length is represented by the symbol "a," which is called as semi-major axis. Conversely, the minor axis indicates the longitudinal axis of the particle; further, half of the minor axis is called the semi-minor axis, which is indicated as "b." If the semi-minor axis "b" is larger than "a," the raindrops become prolate. The parameters "a" and "b" can be used to indicate the shape as well as the size of the raindrop. In this study, the raindrop axis ratio is expressed by "H," which is b/a as shown in Fig. 3.

D. REGIONAL MODELING OF RAINDROP AXIS RATIO

Equations (8), (9), (10), and (11) are given in [13], [17], [21], and [22], respectively.

$$H = 1.03 - 0.062D(1 \le D \le 9\ mm) \tag{8}$$

$$H = 1.0048 + 0.00057D - 0.02628D^2 + 0.003682D^3 - 0.0001677D^4(1 \le D \le 7\ mm) \tag{9}$$

$$H = 0.9951 + 0.02510D - 0.03644D^2 + 0.005030D^3 - 0.0002492D^4(1 \le D \le 8\ mm) \tag{10}$$

$$H = 0.997845 - 0.02082475D - 0.0101085D^2 + 0.000643316D^3(0.5 \le D \le 7\ mm) \tag{11}$$

D stands for the raindrop diameter. Equations (8), (9), and (10) were measured at specific locations in the United States of America [17], [21], [22], and (11) was measured at Daegu, Korea [13]. Using (10) to (11), we compared the axis ratio of raindrops for different regions and the resulting graph is shown in Fig. 4. The raindrop axis ratio H was considered according to the diameter of the raindrops. The plotted graph lines all show similar trends; however, it can be seen that there are certain differences in the shape of raindrops, depending on the region. In small raindrops, the axis ratio of all raindrops is close to 1, indicating that the shape of the raindrops is closer to the spherical shape. Further, as the diameter increases,

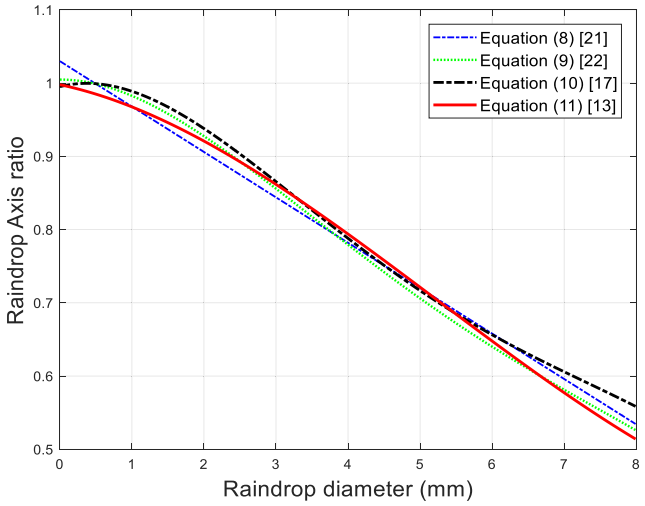

FIGURE 4. Raindrop axis ratio according to drop diameter for different regions [13], [17], [21], [22].

the axis ratio becomes smaller. As an example, the axis ratio of the raindrop according to (10) is larger than that according to (11) in the same drop diameter. More specifically, this observation indicates that the shape of raindrops in the region given in (11) is relatively more oblate than that is given in (10) when the raindrop diameter is smaller than 3 mm or larger than 5.5 mm [13]. Using these features, this study considered the shape and size of raindrops.

IV. THEORY FOR SCATTERING EFFECTS

When light encounters raindrops in the air, various physical phenomena occur. These phenomena can be understood by considering the raindrops as particles. In general, particles illuminated by light demonstrate reflection and refraction, absorption, and scattering. When the light collides with the particles, energy can be dissipated around them and this phenomenon is called scattering. The strength of the scattering strongly depends on the particle size. As shown in Fig. 5, the scattering angle (φ) of a large particle is smaller than the scattering angle (φ') of a smaller particle.

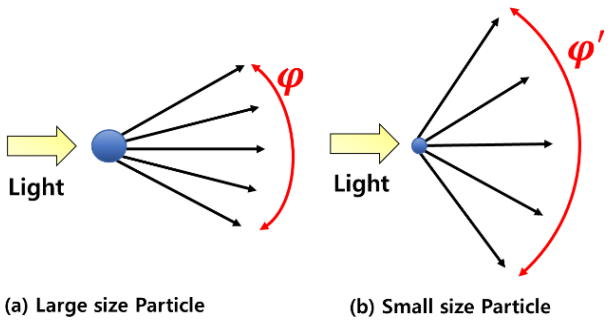

FIGURE 5. Difference in scattering angle according to particle size.

Scattering is divided into elastic scattering, which demonstrates minimal energy exchange between the colliding particles, and inelastic scattering, where significant energy exchange is demonstrated. Common elastic scattering includes Rayleigh and Mie scattering. Rayleigh scattering occurs when particles are much smaller than the wavelength of the light, which is generally not the cases observed in raindrops. Meanwhile, Mie scattering refers light scattered by particles whose diameters is similar or larger than the light wavelength. Consequently, Mie scattering theory is more suitable and was used to model scattering of automotive Lidar in rain conditions [6], [7]. In addition, in such large-sized particles, the strength of the scattering is significantly greater than the strength of the refraction or reflection [9]. Because of these reasons, Mie scattering theory is employed. As explained, these parameters are all considered in this study by characteristics of raindrops.

The Mie theory relies the cross-sectional area of a particle [7], [27]. Generally, efficiencies from various sources are represented as Q_i and can be expressed as shown below:

$$Q_i = \frac{\sigma_i}{\pi r^2} = \frac{\sigma_i}{A} \tag{12}$$

Here, σ_i is the cross-section where scattering occurs from spherical particles of radius r. A means the aperture area of Lidar receiver. The symbol "i" in equation (12) represents the sources of each efficiency. Q_{ext}, Q_{abs}, and Q_{sca} indicate the extinction, absorption, and scattering efficiencies, respectively. Note that [28]

$$Q_{ext} = Q_{sca} + Q_{abs}, \sigma_{ext} = \sigma_{sca} + \sigma_{abs} \tag{13}$$

Generally, for the 905 nm wavelength used in automotive Lidar sensors, scattering is known to be dominantly affected by attenuation [29], and thus, the attenuation by absorption of raindrops was ignored in this study.

V. ANALYSIS OF REGIONAL RAIN ENVIRONMENTS

A. SELECTION AND CLASSIFICATION OF RAIN DATA

Among the regional rain data, this study selects three representing rain models, shown in Table 1. The selected models were derived either from the data measured by a disdrometer or using the data compatible with the disdrometer estimates. The disdrometer has several advantages in the RSD measurement compared to a dual-polarization radar. The radar has to work with different systems, wavelengths, and data processing modes, and is sometimes not accurately calibrated, causing RSD errors. In addition, a ground clutter can influence on the quality of the radar data.

Model A follows (11) and reference [13], and based on the data measured by 2DVD (2-dimensional video disdrometer) at Daegu, Korea. Model B is given in (10) and reference [17], and based on the data obtained by dual-polarization radar (S-Pol) in the east-central Florida, United States of America. Though, the radar data (used in Model B) revealed a small difference in key parameters, including the reflectivity (Z) and differential reflectivity (Z_{dr}), compared to their disdrometer estimates. Additively, Model C is also included, because the model is known to be used the driving simulator PreScan [30]. This model is based on the data from a totally different

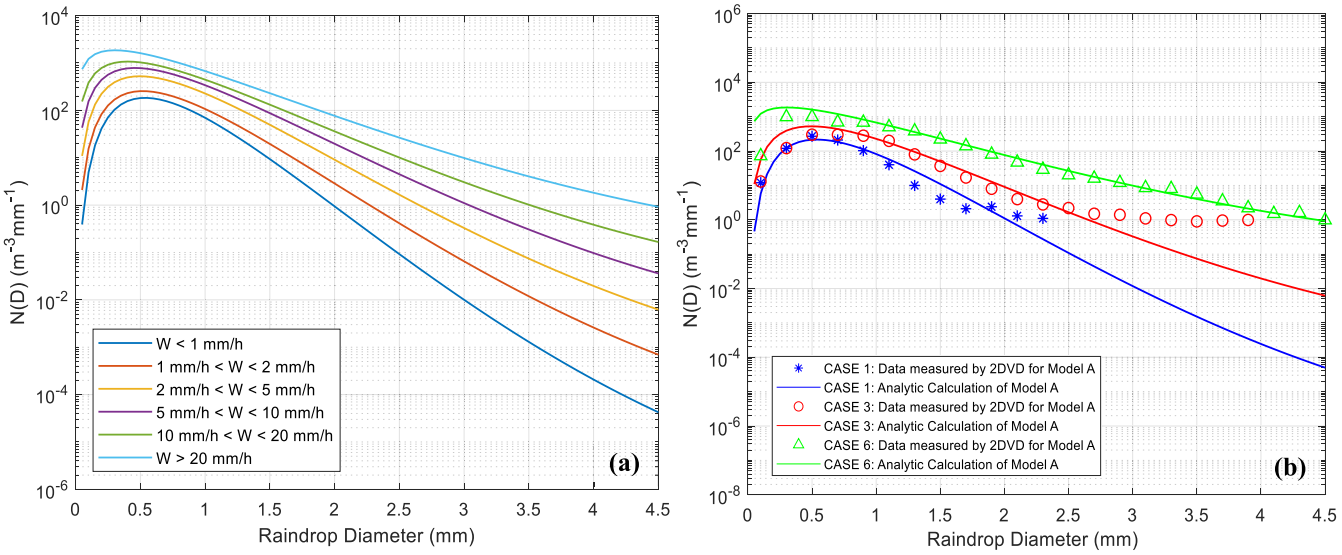

FIGURE 6. (a) Raindrop size distribution using the analytic model considering raindrop axis ratio in a rain environment [13], (b) Comparison of measured data with the analytic results.

TABLE 1. Selected raindrop models.

Raindrop Model	Description
Model A	Model defined by Kim, Suk, Park Lee, and Ko [13] · Considered the raindrop axis ratio · Based on data measured at Daegu, Korea
Model B	Model defined by Brandes, Zhang, and Vivekanandan [17] · Considered the raindrop axis ratio and · Based on data measured at Florida, USA
Model C	Model defined by Tokay and Short [31] · Not considered the raindrop axis ratio · Based on data measured at Kapingamarangi Atoll of Federated States of Micronesia (Pacific Ocean)

TABLE 2. Classification of rain rates (W) following a reference [31].

CASE	Rain rate, W (mm/h)
CASE 1	$0 < W < 1$
CASE 2	$1 < W < 2$
CASE 3	$2 < W < 5$
CASE 4	$5 < W < 10$
CASE 5	$10 < W < 20$
CASE 6	$W > 20$

region, Western Pacific Ocean. The model data is measured at Kapingamarangi Atoll of Federated States of Micronesia by a RD-69 Distromet disdrometer [31].

This model provides the three RSD parameters (N_0, μ, and Λ) but do not include raindrop shape information.

The rain rates W were classified into six cases based on the strength of the rainfall, as proposed by [31]. As listed in Table 2, Cases 1 and 2 commonly depict light rain, ranging from 0 mm/h to 1 mm/h and 1 mm/h to 2 mm/h, respectively. Case 3 defines moderate rain with a range from 2 mm/h to 5 mm/h. Cases 4 and 5 indicate heavy rain ranging from 5 mm/h to 10 mm/h and 10 mm/h to 20 mm/h, respectively. Case 6 represents extreme rain with more than 20 mm/h.

B. CHRACTERISTICS OF REGIONAL RAIN ENVIRONMENTS

This section characterizes the analytic models describing regional rain environments in Table 1. First, Figure 6 characterizes Model A, which is compared with the model B in Fig. 7.

Figure 6(a) illustrates the analytically calculated raindrop size distributions of Model A for the six rain-rate cases in Table 2. The R value is the average of the rain rate range in each case. Raindrop diameter range is set from 0 to 4.5 mm, considering that the diameter of a raindrop greater than 4 mm would easily break down into a small diameter in the atmosphere, referring Fig. 2. Herein, an oblate raindrop shape exampled in Fig. 3 is considered as a spherical raindrop having an equivalent volume, because their scattering effects were reported to be similar [32], [33]. As a result, in this analysis, the scattering of an oblate raindrop becomes weaker than a spherical raindrop whose diameter is the same with the semi-major axis diameter of the oblate one. This weakened scattering in oblate raindrops is commonly observed [32]. In the figure, as the diameter increases, the $N(D)$ value increases temporarily and then decreases again. Regardless of the rain rate, at a diameter of 0.5 mm or more, the value of the distribution increases as the rain rate increases. However, the rate of $N(D)$ reduction with increasing diameter tends to become more gradual.

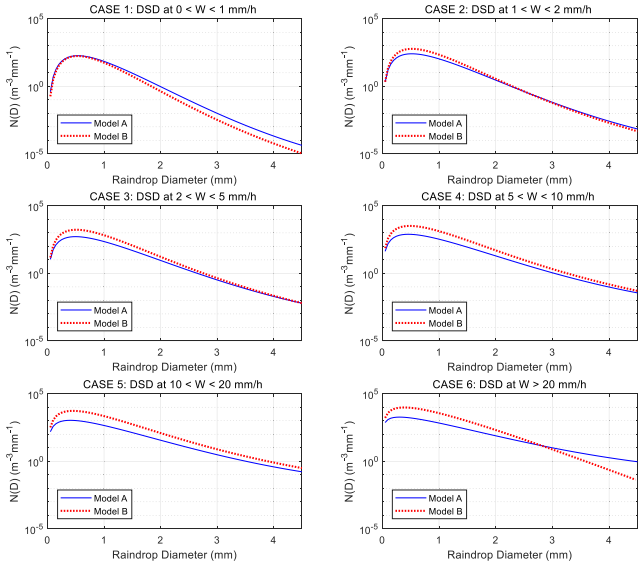

FIGURE 7. Comparison of regional distribution by rain rates.

Figure 6(b) compares the analytic model with the measured data used to develop Model A [13], to observe the reliability of the calculated RSD. The points indicate the data measured by 2DVD and the solid line is the analytic graph derived from Model A. Three analyzed rain-rate cases are colored in blue, red, and green. The overall propensity was consistent when the actual value was compared using an analytic graph. In particular, the measurement and analytic values when the diameter of the raindrop ranged from 0.5 mm to 2 mm were almost identical. In case 6 (W $>$ 20 mm/h), the two values were the same, except when the raindrop diameter was very small (D $<$ 0.5 mm). This is similar to case 4 (5 mm/h $<$ W $<$ 10 mm/h), except the measured $N(D)$ value did not notably decrease at raindrop diameters larger than 2.5 mm. In case 1 (W $<$ 1 mm/h), there were not many data points; however, they were well matched with the analytic graph.

Figure 7 shows the comparisons between Model A and each case of Model B, which was calculated using (10). Model A is represented by a blue solid line and Model B by a red dotted line. Both models demonstrated an increase in the number of raindrops that make up the RSD as the rain rate increased. In cases 1 and 2, where the rain rate was low, the RSD of Models A and B were similar to each other. However, when the rain rate increased, the distribution of Model B in small raindrop diameters (D $<$ 2 mm) was larger than Model A and the difference becomes more obvious. In case 6, which has a severe rain environment, Model B demonstrated larger distributions at diameters less than 3 mm. It can be observed that the difference in the diameters of the raindrops according to the region is exceptional. Thus, it is anticipated that the performance of Lidar sensors would vary by regions, owing to their difference in raindrop shape, size, and distribution, which consequently leads to different scattering magnitude.

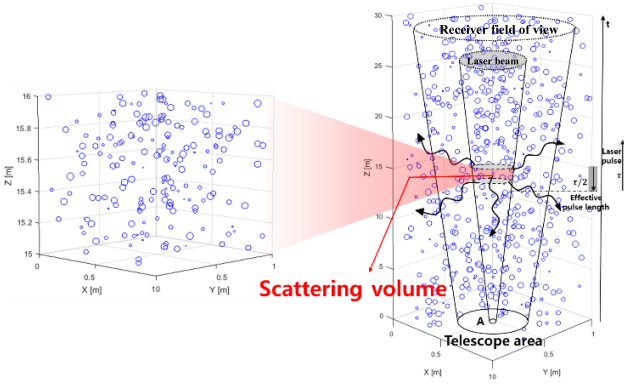

FIGURE 8. Illustration of the Lidar geometry in RD [36].

VI. MODELING OF LIDAR SENSORS

A. CONCEPT OF LIDAR SENSOR MODEL

For the performance evaluation of the Lidar sensor in the rain environment, a Lidar sensor model was developed. The model starts with governing equations that are widely employed in automotive Lidar analysis [34], and then implemented with the aforementioned raindrop models. For reliable analysis, the model parameters were derived from the specifications of a commercial Velodyne's Lidar Puck (VLP-16) [35]. The performance of the Lidar model was determined by comparing the received signal power with the change in rain environment. The transmitting power used in this paper was determined to use the pulse duration and pulse energy in Lidar specifications.

B. GOVERNING EQUATIONS OF LIDAR SENSOR MODEL

Figure 8 illustrates the scattering effects on the Lidar performance according to the raindrop distribution in space [36]. Among the spaces distributed with different sizes of raindrops, the space through which the laser beam penetrates is influential. There are several ways to detect an object using a Lidar sensor. Among the Lidar sensors commonly used in vehicles, the time-of-flight measurement method is widely used to obtain the distance as follows.

$$R = \frac{t_{receive} - t_{send}}{2} = \frac{c\Delta t}{2} = \frac{c\tau}{2} \tag{14}$$

The distance R can be obtained by measuring the time ($\Delta t = t_{receive} - t_{send}$) taken for the laser pulse to travel from the transmitter until the laser pulse is reflected back from the particular object. c is the speed at which light travels through the air. τ is the travel time; thus, one half of the travel time was consumed to reach the target and another half was the return time of the reflected light.

The signal received on the Lidar sensor can be expressed according to (15). The power P is the power when the laser pulse returns from the distance of travel, R, which consists of four major variables [34].

$$P(R) = K \times G(R) \times \beta(R) \times T(R) \tag{15}$$

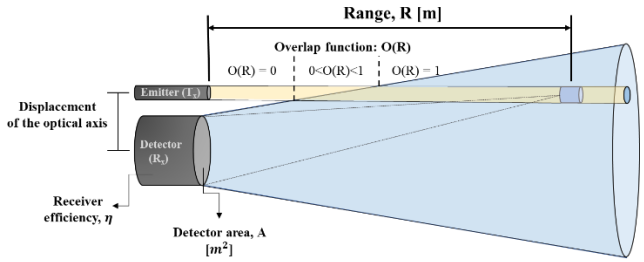

FIGURE 9. Representation of overlap area considering to range *R* [34].

Each variable of (15) is explained below. The first variable, K, represents the overall performance of the Lidar sensor system and is calculated by the following equation:

$$K = P_0 \frac{c\tau}{2} A\eta \tag{16}$$

P_0 is the average power of the laser pulse from a Lidar emitter. P_0 and τ values were determined using the datasheets of the Velodyne LiDAR [35]. Here, $c\tau/2$ indicates the length of the volume that has been illuminated by the laser pulse at any random time [16]. η and A are the overall system efficiency and the area of the Lidar receiver, respectively.

The second variable $G(R)$ is a geometrical element that can be represented as a crossover function. As shown in Fig. 9, there are overlapping areas where light is detected by the beam field-of-view of each transmitter and receiver. This area is indicated by the object function $O(R)$ and is determined according to the distance R; the formula for calculation is as presented below:

$$G(R) = \frac{O(R)}{R^2} \tag{17}$$

$O(R)$ determines the overlapping area between the area observed by the receiver, which depends on the distance from the object. This area can be divided into three zones shown in Fig. 9. The first zone, $O(R) = 0$, indicates that there is no overlapping area between the optical channels of the transmitter and the receiver. The second zone ($0 < O(R) < 1$) is the area where the cross section of the transmitter beam partially overlaps the cross section of the received beam. Lastly, when $O(R) = 1$, the optical channels of the receiver and transmitter perfectly overlap [7]. This study considers area overlapping completely.

The third part of (15), $\beta(R)$, stems from the backscattering size of raindrops. Because it indicates backscattering, it occurs in the opposite direction to the transmitting laser pulse, i.e., at a scatting angle of 180°. Using (14), the backscattering coefficients can be obtained and the following as:

$$\beta(R) = \frac{c\tau}{2} \times \sum\nolimits_{unit} (\sigma_{sca} \times n_{sca}) \tag{18}$$

Here, σ_{sca} indicates a cross section, as described in (13). n_{sca} indicates the number of particles of various sizes that are scattered by laser pulses per unit volume.

Finally, $T(R)$ is the transmittance determining the reduction in the light intensity of the transmitting laser beam owing to its journey over distance R.

$$T(R) = exp[-2\int_0^R \alpha(r,\lambda)dr] \tag{19}$$

This equation was modified to fit the Lidar sensor system using Lambert–Beer–Bouguer law [37]. Any attenuation occurring at a distance R from the Lidar sensor (owing to an object in the transmission path) indicates light extinction. Therefore, $\alpha(r, \lambda)$ can be defined as an extinction coefficient. Also, $T(R)$ is expressed using the extinction coefficient α and the distance R from the particle.

$$T(R) = exp(-2\alpha R) \tag{20}$$

The following governing equation of the Lidar sensor can be obtained by substituting the expression in (15) by the above four variables [34]:

$$P_r(R,\lambda) = \left[P_0 \frac{c\tau}{2} A\eta\right] \times \left[\frac{O(R)}{R^2}\right] \times \left[\frac{1}{4\pi} \sum_{unit} \sigma_{sca} * n_{sca}\right] \times \left[exp\left\{-2\int_0^R \alpha(r,\lambda)dr\right\}\right] \tag{21}$$

Using (21), the Lidar sensor model was implemented using MATLAB & Simulink software. It consists of four parts corresponding to the four variables of (15). The four parts are eventually multiplied to represent the performance of the Lidar sensor, which is expressed by the received signal power of a laser pulse, P_r. By linking these Lidar sensor model with the previously implemented RDs, sensor performances were compared according to regions.

VII. RESULTS AND DISCUSSIONS

A. SIMULATION SCENARIO OF VEHICLE DRIVING

The developed Lidar sensor model was validated using the PreScan driving simulation software. Figure 10 illustrates one of the simulation scenarios. The driving simulation generates the distance between the two vehicles. The host vehicle has a Lidar sensor targeting the target vehicle. The distance information is then fed to each Lidar sensor model containing the

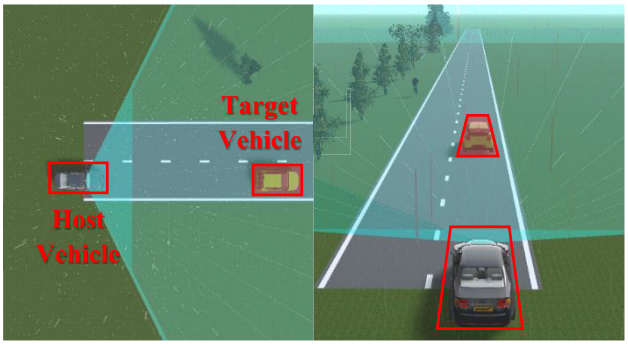

FIGURE 10. Vehicle scenario: Distance control and maintaining the lane (left: top view, right: forward view).

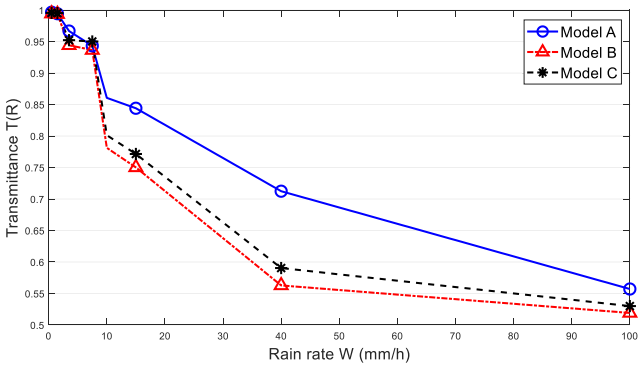

FIGURE 11. Comparison of transmittance by each model according to the rain rates W.

RD of different regions (i.e., Models A, B, and C in Table 1). As shown in (21), the distance between the vehicles can provide the received power at each raindrop environment. It is to be noted that we mainly focused on the reduction of received signal power for each rain environment. The reduced power would alter the signal to noise ratio of the Lidar sensor, influence its detection threshold, and degrade the perception performance of ADAS systems [38].

B. DEGRADATION IN LIDAR SENSOR PERFORMANCES

As discussed in section V-B, the rain environment varies from region to region. Therefore, there are differences in the composition of raindrops, which affects the amount of scattering depending on the amount of rain rates. This effect was quantitatively derived through the extinction coefficient parameter, which affects the transmittance of the Lidar sensor. Thus, the performance of Lidar according to rain rates was derived. Next, we compared the three models according to the region. As discussed above, Model A is a Lidar model that was developed using (11), based on the results measured in Daegu, Korea, while Model B represents Florida, United States. Further, the size, number, and shape of the raindrops were considered as environmental variables. Model C is a distribution implemented based on the data measured in Kapingamarangi Atoll of Federated States of Micronesia [32]. Model C experimentally presented the N_0, μ, and Λ values required to implement probability distributions.

Figure 11 is a transmittance $T(R)$ in (19) or (20), which reflects the regional rain environments. In all three models, the transmittance decreases as the rain rate increases, as expected. This is because the number of raindrops that make up their distribution increases, as shown in Fig. 7, which also results in more scattering of raindrops. Moreover, the transmittance of Model A has a value greater than Model B. According to Fig. 4, Model B has relatively spherical-shaped raindrops when compared to Model A. As the raindrops become more spherical, the scattering magnitude increases [32]. In addition, as shown in Fig. 7, the distribution of raindrop in Model A is smaller, compared to the RD of Model B when rain rates increase. These are

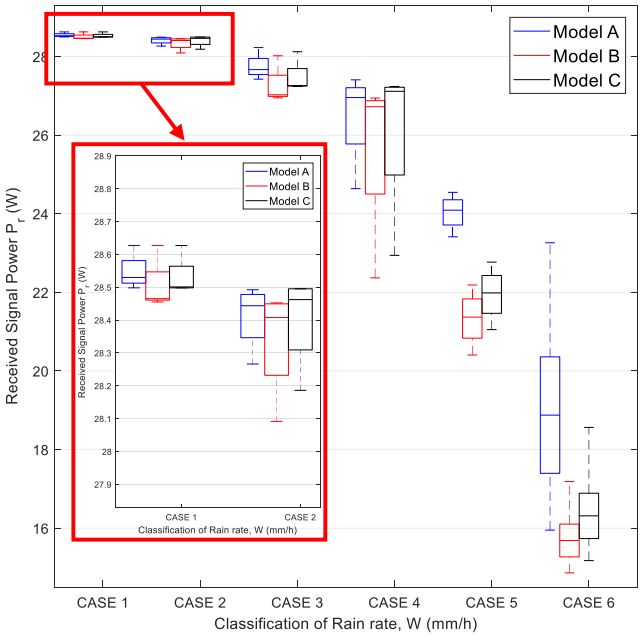

FIGURE 12. Comparison graph of received Lidar signal power based on regional RD according to rain rates.

why Model B having more attenuated transmittance than Model A.

The calculated transmittance is now converted to the received signal power of the Lidar sensor symbolled by P_r in (21). Figure 12 compares the received signal powers of the three regional rain models corresponding to rain rates. In all models, the received signal power is attenuated as the rain rate increased. When the rain rate was small (cases 1, 2), the differences between the three models was not significant. As an example, for case 1, the values of average received signal power for the models were 28.53 W, 28.47 W, and 28.50 W, respectively. However, as the rain rate increased, the three models demonstrated considerable differences; moreover, the degree of difference varied from model to model. In case 6, Model A had 20.40 W, Model B had 16.11 W, and Model C had 16.90 W of received signal power. This differed by 11.27 W (35.59%), 15.56 W (49.13%), and 14.77 W (46.64%), respectively, when compared to the transmitting power, 31.67 W. Therefore, it can be observed that the Lidar received signal power was significantly affected by local characteristics, especially, in the case of heavy rain rates. While analyzing the three models more elaborately, Model B demonstrated the greatest degree of attenuation in received signal power while Model A relatively demonstrated the lowest degree of attenuation. Interestingly, Model C demonstrated a trend similar to Model B, with a maximum difference of ∼0.7 W. Therefore, the regional rain environments critically impact on sensor-level performances.

C. DISCUSSION

In general, the detection threshold of Lidar sensors largely determines their detection errors [39], [40]. With a high

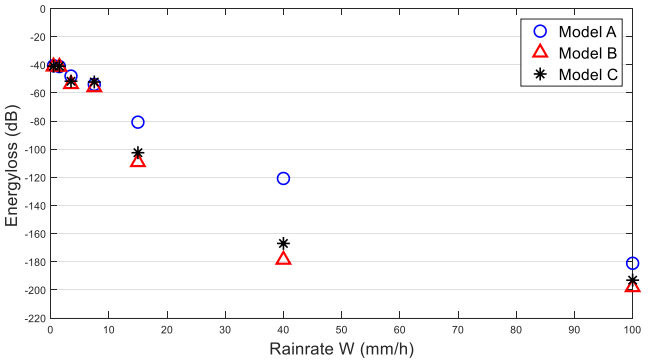

FIGURE 13. Comparison of the energy loss of each model according to the rain rates.

threshold, the risk of missed warnings increases. If the detection threshold goes low, the missed warming is improved but the possibility of false alarms increases. As an example, a vehicle is driving in the case 5 (i.e., 10 mm/h $<$ W $<$ 20 mm/h) and its detection threshold happens to set to be 23 W by the manufacturer. As shown in Fig. 12, if the vehicle is in region A, its ADAS system can detect the target object, which cannot be detectable when the same vehicle is driving in region B or C. As a solution, the detection threshold is assumed to be lowered to 16W and the ADAS system is now detectable in all three regions. However, if the rain becomes heavier and the rain rate is increased to be case 6, the same Lidar can detect the object in region A, cannot detect in region B, and may or may not detect in region C. To solve this regional dependency, the threshold should be further decreased. However, as noted, the low threshold easily leads to false alarm.

Another noteworthy point is that the case 6 (W $>$ 20mm/h) is a heavy rain but not an extreme environment like a squall. According to Korea Meteorological Administration (KMA, Korea) [41], the maximum rain rate on July and August is always larger than 20 mm/h and reaches 68 mm/h when measured from 2010 to 2019 (except one exception of 11.5 mm/h measured on August 2016). Therefore, it is important to optimally design the detection threshold with seriously considering the regional impact.

The transmittance values in Fig. 11 are applied to the PreScan driving software because the PreScan does not include Lidar models specially designed to include rain effects. The updated driving simulation provides a parameter named energy loss, which is defined to be the ratio between the received and transmitted powers. Figure 13 depicts a tendency similar with what observed beforehand. As the rain rate increases, the energy loss increases, implying that less light is transmitting than the light being introduced. In addition, the level of energy loss strongly depends on rain models and regional environments.

VIII. CONCLUSION

In this paper, the Lidar sensor in rain environments was modeled and quantitatively evaluated, while considering the reginal raindrop distributions. The rain environment of each region was modeled using a CG model, imported to a custom-built Lidar sensor model, and quantitatively compared based on its effects on the Lidar performance degradation. The regional rain environment was characterized using the factors affecting scattering, including the sizes, numbers, and shapes of raindrops. It is considered that the scattering of a spherical raindrop is stronger than that of an oblate raindrop. As all these characteristics differ by different regions, it was expected that the Lidar performance depends on the regional raindrop distribution. The regional impact was embedded in our Lidar model, which was developed using the MATLAB & Simulink. In addition, the Lidar model was equipped in a automobile driving simulation. The simulation results demonstrated that the Lidar received signal power showed variations in the attenuation for different regions. Therefore, the regional impact is crucial to Lidar performance degradation in rain environment, and should be carefully examined in Lidar sensor or ADAS system design.

REFERENCES

[1] R. Changalvala and H. Malik, "LiDAR data integrity verification for autonomous vehicle," *IEEE Access*, vol. 7, pp. 138018–138031, 2019.
[2] H. Gao, B. Cheng, J. Wang, K. Li, J. Zhao, and D. Li, "Object classification using CNN-based fusion of vision and LiDAR in autonomous vehicle environment," *IEEE Trans. Ind. Informat.*, vol. 14, no. 9, pp. 4224–4231, Sep. 2018.
[3] M. Konrad and M. Schramm, "Validation of ADAS by sensor fusion," *ATZ Worldwide*, vol. 120, no. 6, pp. 56–59, Jun. 2018.
[4] J. Zeisler and H.-G. Maas, "Analysis of the performance of a laser scanner for predictive automotive applications," *ISPRS Ann. Photogramm., Remote Sens. Spatial Inf. Sci.*, vol. 2, pp. 49–56, Aug. 2015.
[5] S. Hasirlioglu, A. Kamann, I. Doric, and T. Brandmeier, "Test methodology for rain influence on automotive surround sensors," in *Proc. IEEE 19th Int. Conf. Intell. Transp. Syst. (ITSC)*, Nov. 2016, pp. 2242–2247.
[6] R. H. Rasshofer, M. Spies, and H. Spies, "Influences of weather phenomena on automotive laser radar systems," *Adv. Radio Sci.*, vol. 9, pp. 49–60, Jul. 2011.
[7] M. Berk, M. Dura, J. V. Rivero, O. Schubert, H. M. Kroll, B. Buschardt, and D. Straub, "A stochastic physical simulation framework to quantify the effect of rainfall on automotive LiDAR," SAE Tech. Paper 2019-01-0134, 2019.
[8] T. Fersch, A. Buhmann, A. Koelpin, and R. Weigel, "The influence of rain on small aperture LiDAR sensors," in *Proc. German Microw. Conf. (GeMiC)*, Mar. 2016, pp. 84–87.
[9] S. Hasirlioglu and A. Riener, "Introduction to rain and fog attenuation on automotive surround sensors," in *Proc. IEEE 20th Int. Conf. Intell. Transp. Syst. (ITSC)*, Oct. 2017, pp. 1–7.
[10] S. Hasirlioglu and A. Riener, "A model-based approach to simulate rain effects on automotive surround sensor data," in *Proc. 21st Int. Conf. Intell. Transp. Syst. (ITSC)*, Nov. 2018, pp. 2609–2615.
[11] C. Goodin, D. Carruth, M. Doude, and C. Hudson, "Predicting the influence of rain on LiDAR in ADAS," *Electronics*, vol. 8, no. 1, p. 89, Jan. 2019.
[12] T. H. Raupach and A. Berne, "Retrieval of the raindrop size distribution from polarimetric radar data using double-moment normalisation," *Atmos. Meas. Techn.*, vol. 10, no. 7, pp. 2573–2594, 2017.
[13] H.-L. Kim, M.-K. Suk, H.-S. Park, G.-W. Lee, and J.-S. Ko, "Dual-polarization radar rainfall estimation in korea according to raindrop shapes obtained by using a 2-D video disdrometer," *Atmos. Meas. Techn.*, vol. 9, no. 8, pp. 3863–3878, Aug. 2016.
[14] G. Zhang, J. Vivekanandan, and E. Brandes, "A method for estimating rain rate and drop size distribution from polarimetric radar measurements," *IEEE Trans. Geosci. Remote Sens.*, vol. 39, no. 4, pp. 830–841, Apr. 2001.
[15] Weather Radar Center. *Principle of Radar Observation*. Accessed: Aug. 14, 2019. [Online]. Available: http://radar.kma.go.kr/lecture/radar/principle.do

[16] V. N. Bringi and V. Chandrasekar, *Polarimetric Doppler Weather Radar: Principles and Applications*. Cambridge, U.K.: Cambridge Univ. Press, 2001.
[17] E. A. Brandes, G. Zhang, and J. Vivekanandan, "Experiments in rainfall estimation with a polarimetric radar in a subtropical environment," *J. Appl. Meteorol.*, vol. 41, no. 6, pp. 674–685, Jun. 2002.
[18] C. W. Ulbrich, "Natural variations in the analytical form of the raindrop size distribution," *J. Climate Appl. Meteorol.*, vol. 22, no. 10, pp. 1764–1775, Oct. 1983.
[19] X. Liu, Q. Wan, H. Wang, H. Xiao, Y. Zhang, T. Zheng, and L. Feng, "Raindrop size distribution parameters retrieved from guangzhou S-band polarimetric radar observations," *J. Meteorol. Res.*, vol. 32, no. 4, pp. 571–583, Aug. 2018.
[20] G. Zhang, *Weather Radar Polarimetry*. Boca Raton, FL, USA: CRC Press, 2016.
[21] H. R. Pruppacher and R. L. Pitter, "A semi-empirical determination of the shape of cloud and rain drops," *J. Atmos. Sci.*, vol. 28, no. 1, pp. 86–94, Jan. 1971.
[22] K. V. Beard and R. J. Kubesh, "Laboratory measurements of small raindrop distortion. Part 2: Oscillation frequencies and modes," *J. Atmos. Sci.*, vol. 48, no. 20, pp. 2245–2264, Oct. 1991.
[23] G. Kathiravelu, T. Lucke, and P. Nichols, "Rain drop measurement techniques: A review," *Water*, vol. 8, no. 1, p. 29, Jan. 2016.
[24] A. W. Green, "An approximation for the shapes of large raindrops," *J. Appl. Meteorol.*, vol. 14, no. 8, pp. 1578–1583, Dec. 1975.
[25] S. Asano and G. Yamamoto, "Light scattering by a spheroidal particle," *Appl. Opt.*, vol. 14, no. 1, pp. 29–49, 1975.
[26] S. Asano, "Light scattering properties of spheroidal particles," *Appl. Opt.*, vol. 18, no. 5, pp. 712–723, 1979.
[27] Q. Jing, D. Liu, and J. Tong, "Study on the scattering effect of terahertz waves in near-surface atmosphere," *IEEE Access*, vol. 6, pp. 49007–49018, 2018.
[28] C. Mätzler, "MATLAB functions for Mie scattering and absorption, version 2," Institut für Angewandte Physik, Bern, Switzerland, IAP Res. Rep., 2002.
[29] J. M. Khaleel and S. A. Salman, "Calculation of the attenuation of infrared laser beam propagation in the atmosphere," *J. Res. Diyala Humanity*, vol. 37, pp. 81–91, 2009.
[30] (2019). *PreScan, PreScan Applications Datasheet*. [Online]. Available: https://tass.plm.automation.siemens.com/prescan
[31] A. Tokay and D. A. Short, "Evidence from tropical raindrop spectra of the origin of rain from stratiform versus convective clouds," *J. Appl. Meteorol.*, vol. 35, no. 3, pp. 355–371, Mar. 1996.
[32] C. F. Bohren and D. R. Huffman, *Absorption and Scattering of Light By Small Particles*. Hoboken, NJ, USA: Wiley, 2008.
[33] Y. M. Kim, "Prediction model of propagation of the millimeter wave wireless transmission channels in the rain environment," *J. Korea Soc. Comput. Inf.*, vol. 5, no. 4, pp. 55–61, 2000.
[34] T. G. Phillips, N. Guenther, and P. R. McAree, "When the dust settles: The four behaviors of LiDAR in the presence of fine airborne particulates," *J. Field Robot.*, vol. 34, no. 5, pp. 985–1009, Aug. 2017.
[35] (2019). *VLP-16 Puck*. [Online]. Available: http://velodynelidar.com/vlp-16.html
[36] S. C. Weitkamp, Ed., *LiDAR: Range-Resolved Optical Remote Sensing of the Atmosphere*. Berlin, Germany: Springer-Verlag, 2005.
[37] Y. Li, Y. Wang, W. Deng, X. Li, and L. Jiang, "LiDAR sensor modeling for ADAS applications under a virtual driving environment," SAE Tech. Paper 2016-01-1907, 2016.
[38] G. Arisholm, T. Skauli, and S. Landrø, "Combined range ambiguity resolution and noise reduction in LiDAR signal processing," *Opt. Eng.*, vol. 57, no. 7, p. 1, Jul. 2018.
[39] K. Liu, W. Wang, and J. Wang, "Pedestrian detection with LiDAR point clouds based on single template matching," *Electronics*, vol. 8, no. 7, p. 780, Jul. 2019.
[40] A. Ebrahimzadeh, M. Najimi, S. M. H. Andargoli, and A. Fallahi, "Sensor selection and optimal energy detection threshold for efficient cooperative spectrum sensing," *IEEE Trans. Veh. Technol.*, vol. 64, no. 4, pp. 1565–1577, Apr. 2015.
[41] Korea Meteorological Administration. (Jan. 2, 2020). *Rank Statistics Division List*. Accessed: Jan. 2, 2020. [Online]. Available: https://data.kma.go.kr/climate/RankState/selectRankStatisticsDivisionList.do?pgmNo=179

MIJUNG BYEON received the B.S. degree in electronics and computer engineering from Chonnam National University, Gwangju, South Korea, in 2018. She is currently pursuing the master's degree in automotive engineering with Hanyang University, Seoul, South Korea. Her current research interest includes the design and performances analysis of advanced driver assistance system sensors used in autonomous vehicles.

SANG WON YOON (Senior Member, IEEE) received the B.S. degree in electrical engineering from Seoul National University, Seoul, South Korea, in 2000, and the M.S. and Ph.D. degrees in electrical engineering and computer science from the University of Michigan, Ann Arbor, MI, USA, in 2003 and 2009, respectively. From 2009 to 2013, he was a Senior Scientist and a Staff Researcher with the Toyota Research Institute of North America, Ann Arbor, where he conducted research in the fields of power electronics and sensor systems for automobiles. Since 2013, he has been with the Department of Automotive Engineering, Hanyang University, Seoul, where he is currently an Associate Professor. His current research interests include power electronics, sensors and sensor systems, electronic reliability, and their applications in conventional and future vehicles.